JACS Au
AN OPEN ACCESS JOURNAL OF THE AMERICAN CHEMICAL SOCIETY

pubs.acs.org/jacsau
Article

A Self-Immobilizing Photosensitizer with Long-Term Retention for Hypoxia Imaging and Enhanced Photodynamic Therapy

Zifan Zhu, Yun Feng, Qiufen Tian, Jiawen Li, Chencong Liu, Yuchi Cheng, Sanjun Zhang, Yijing Dang, Jing Gao, Yi Lai, Fan Zhang, Haijun Yu, Wen Zhang, and Zhiai Xu*

Cite This: JACS Au 2024, 4, 4032−4042

ABSTRACT: The precise theranostic strategy of fluorescence imaging-guided photodynamic therapy (PDT) can effectively mitigate the adverse effect of photosensitizers in normal cells and tissues. However, low tumor enrichment and high diffusivity of photosensitizers significantly compromise the imaging accuracy and PDT effect. In this study, we have developed a nitroreductase (NTR)-activated and self-immobilizing photosensitizer CyNT-F, which showed enhanced enrichment in tumor tissues and facilitated precise and sustained imaging as well as PDT for hypoxia tumors. mPEG-*b*-PDPA nanomicelles encapsulating photosensitizers underwent dissociation and released CyNT-F in tumor cells. CyNT-F and NTR enzymatically reacted in situ to generate highly reactive quinone methide, subsequently covalently binding to adjacent proteins for fluorescence and PDT activation. CyNT-F exhibited longer intracellular retention (7 days) and effectively inhibited the tumor growth of solid hypoxia tumor. We believe the activatable and self-immobilizing strategy of PDT presents a novel methodology for minimizing the adverse effect and enabling spatiotemporally accurate ablation of diseased cells and tissues.

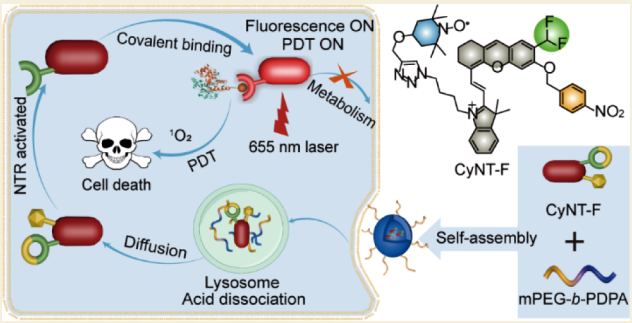

KEYWORDS: *self-immobilizing, activatable photosensitizer, hypoxia, photodynamic therapy, long-term retention*

INTRODUCTION

As one of the most promising stars in the field of cancer treatment, photodynamic therapy (PDT) has gained significant attention in recent years owing to the merits of noninvasiveness, spatiotemporal selectivity, lower side effects, and exceptional therapeutic efficacy.[1−3] A typical PDT process involves pretreating the tumor area with a photosensitizer; then, in the presence of specific light and oxygen molecules, the photosensitizer generates reactive oxygen species (ROS) to cause damage to proteins, nucleic acids, lipids, membranes, and organelles, which can induce cell apoptosis.[4,5] However, traditional photosensitizers lack tumor-targeting ability and exhibit always-on fluorescence and ROS generation under light, resulting in excessive nonspecific signals and potential toxicity to normal tissues, which largely restrict the clinical application of PDT.[6] Activatable photosensitizers that utilize the special microenvironment of tumors to stimulate the photosensitizer can achieve precise differentiation and targeted eradication of tumors.[7−13] The fluorescence signal of these photosensitizers remains quiescent in normal tissues and lacks the ability to generate ROS. Only upon interaction with the tumor site and specific analytes, the fluorescence will be activated, thereby triggering photodynamic activity.[14−20] This "stimuli-triggered activation" strategy shows great promise in reducing the side effects of PDT. However, the majority of current activatable photosensitizer designs rely on the incorporation of heavy atoms, thereby augmenting the inherent dark toxicity of photosensitizers.[21−25]

A further challenge of traditional small molecule photosensitizers is that they readily exit their target cells and then enter the surrounding normal cells due to the rapid metabolism of tumor tissues, which hampers substantial accumulation and long retention of photosensitizers at the tumor site.[26−34] Meanwhile, hypoxia is one of the vital characteristics of the tumor microenvironment.[35−37] Nevertheless, as photosensitizers require oxygen consumption to generate ROS, the hypoxia environment becomes an adverse factor that affects the efficacy of PDT to some extent.[38−40] Therefore, enhancing the photodynamic efficiency of photosensitizers in hypoxic tumors poses a significant challenge.

In recent decades, significant endeavors have been dedicated to augmenting the efficacy of PDT in cancer treatment.[41,42] For instance, nanodelivery strategies were developed by

Received: August 28, 2024
Revised: September 18, 2024
Accepted: September 19, 2024
Published: October 3, 2024

https://doi.org/10.1021/jacsau.4c00787
JACS Au 2024, 4, 4032−4042

Scheme 1. (A) Schematic Illustration of the Molecule Design of the Nitroreductase (NTR)-Activatable and Self-Immobilizing Photosensitizer CyNT-F; (B) The Mechanism of NTR-Activated Protein Binding and Micelle Dissociation; (C) Schematic Illustration of NTR-Activated Self-Immobilizing Photosensitizer to Achieve Photodynamic Therapy of Hypoxia Tumor

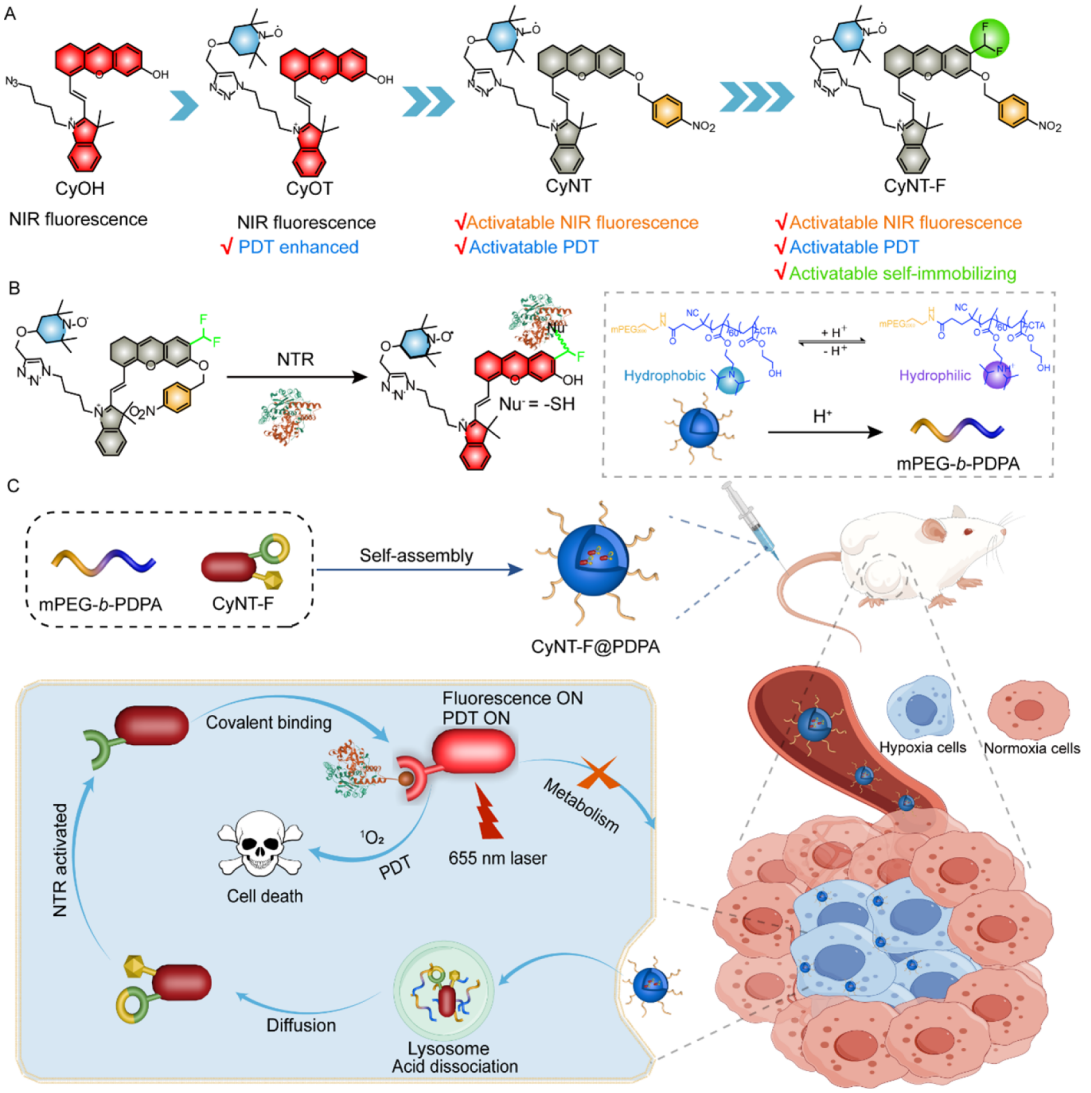

employing passive targeting based on the enhanced permeability and retention (EPR) effect,[43−45] or active targeting using specific ligands to enhance tumor accumulation and photosensitizer retention. Through response-induced small molecule in situ self-assembly and nanoscale structure formation, enhanced cellular uptake and retention have been achieved.[46,47] Additionally, there have been strategies aimed at mitigating tumor hypoxia and augmenting photodynamic efficacy through oxygen supplementation.[48−52] Despite significant improvement, the challenge of inadequate interaction between small molecule photosensitizers and tumor cells, as well as their facile diffusion, limits the imaging resolution and PDT efficacy at the in vivo level.

To address the above issues in PDT, inspired by the bioorthogonal labeling strategy,[53,54] we herein proposed a stimulus-triggered self-immobilizing strategy that effectively reduced the diffusion of the photosensitizer by augmenting its binding affinity to cellular proteins. 2,2,6,6-Tetramethylpiperidinyloxy (TEMPO, a stable free radical group) was first connected to hemicyanine to enhance the singlet oxygen yield.[55,56] Subsequently, the hydroxyl group of hemicyanine was *ortho*-modified with a leaving group (difluoromethyl), and the hydroxyl group was modified with a 4-nitrobenzyl moiety to serve as the recognition site for nitroreductase (NTR), which quenched the fluorescence and PDT of the photosensitizer. A precursor of difluoro-modified quinone methide was introduced at the *ortho*-position of the hemicyanine hydroxyl group. Upon enzymatic stimulation, electrophilic quinone methide formed, which covalently binds to nucleophilic groups on nearby proteins to activate fluorescence and PDT. This covalent binding strategy enabled precise identification and elimination of tumor cells at high resolution. Finally, photosensitizers were encapsulated in polymers (mPEG-*b*-PDPA) to facilitate the targeted treatment of solid tumors in vivo. The activated photosensitizer could accumulate and retain within the tumor for a prolonged period due to the limited permeability of macromolecular proteins across cell membranes, effectively inhibiting tumor growth (Scheme 1).

RESULTS AND DISCUSSION

We undertook a systematic rational design and chemical modification approach based on the fundamental structure of

https://doi.org/10.1021/jacsau.4c00787
JACS Au 2024, 4, 4032−4042

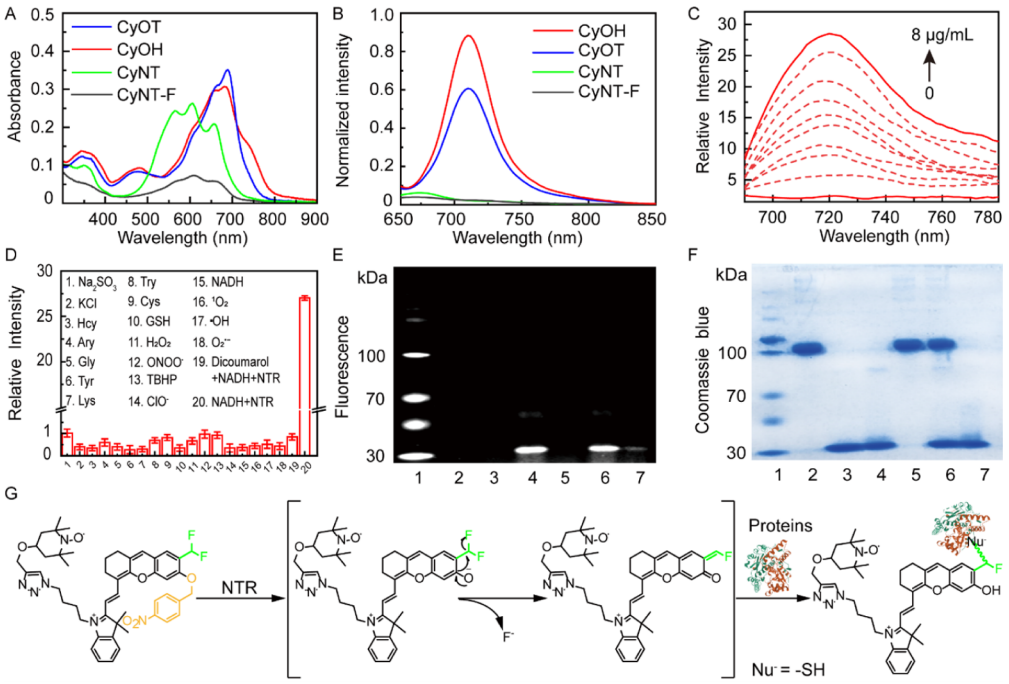

Figure 1. (A,B) Absorption (A) and fluorescence (B) spectra of CyOH, CyOT, CyNT, and CyNT-F in PBS solution. λ_{Ex} = 640 nm. (C) Concentration-dependent response of CyNT-F to NTR (λ_{Ex} = 680 nm, 0−8 μg/mL). (D) Fluorescence selectivity of CyNT-F toward NTR and potential interferents (mean ± SD, n = 3). (E) Protein fluorescence imaging and Coomassie blue staining (F) of SDS-PAGE gel. NTR or BSA (bovine serum albumin) was incubated with or without probes in PBS solution at 37 °C for 2 h. 1. Marker, 2. BSA, 3. NTR, 4. CyNT-F+NTR, 5. CyNT-F+BSA, 6. CyNT-F+BSA+NTR, 7. CyNT+NTR. (G) NTR response and protein labeling mechanism of CyNT-F.

hemicyanine azide-derivative CyOH. Firstly, the nitrophenyl group was introduced to quench the fluorescence of CyOH, followed by the introduction of the difluoromethyl group as a quinone methyl precursor to confer covalent properties upon the probe. Finally, TEMPO was conjugated to the probe via click chemistry as a photosensitizer enhancement unit for PDT to obtain CyNT-F. The detailed synthetic routes of CyNT-F and control probes (CyOH, CyOT, and CyNT) are illustrated in Schemes S1−S3, and the structures of these compounds were characterized by NMR spectra and high-resolution mass spectra (HRMS), verifying their successful synthesis (Figures S1−S15).

With these compounds in hand, the optical properties of CyOH, CyOT, CyNT, and CyNT-F were first characterized through UV−vis and fluorescence spectra. As depicted in Figure 1A, CyOH exhibited maximum absorption and emission peaks at 670 and 710 nm, respectively. Similar absorption and emission spectra were observed for CyOT modified with TEMPO. However, the maximum absorption peaks of CyNT and CyNT-F modified with nitrobenzene and difluoromethyl groups had a significant blue shift. More importantly, the fluorescence of CyNT and CyNT-F was substantially quenched, which could be attributed to the weakened intramolecular charge transfer (ICT) effect in hemicyanine due to phenolic hydroxyl group protection (Figure 1B). Subsequently, the UV−vis-NIR absorption and fluorescence response of CyNT-F to NTR was evaluated in a phosphate-buffered saline (PBS) solution. Upon coincubation with NTR, the absorption peak of CyNT-F exhibited a red shift (Figure S16), which was similar to the absorption peak of CyOT, indicating successful elimination of nitrobenzene through enzymatic reaction and effective restoration of the hydroxyl group. Moreover, the fluorescence intensity at 720 nm gradually increased with the increasing NTR concentration, demonstrating a strong linear correlation within the range of 0−2.5 μg/mL enzyme concentration (R^2 = 0.9899) (Figures 1C and S17). The time-dependent curve revealed that equilibrium was achieved within 10 min upon the addition of NTR (Figure S18). Selectivity and interference experiments demonstrated robust specificity and anti-interference properties of CyNT-F toward NTR (Figures 1D and S19), and CyNT-F exhibited significant fluorescence enhancement for NTR in a wide range of pH (6.0−8.0) solutions (Figure S20), suggesting that CyNT-F was suitable for NTR detection in physiological environments. Additionally, under identical experimental conditions, the response of CyNT to NTR displayed similar spectral characteristics to CyNT-F (Figure S21).

Encouraged by the rapid response and excellent specificity of the probe to NTR, we further studied the ability of CyNT-F to covalently label proteins after the enzymatic reaction. CyNT-F and CyNT were incubated with NTR or BSA, followed by the analysis of fluorescence labeling of proteins. As depicted in Figure 1E,F, NTR treated with CyNT-F exhibited strong fluorescence, while no fluorescence signal was observed in the CyNT-F+NADH group or NTR group. Furthermore, upon incubation of NTR and BSA (a competing protein) with CyNT-F for 30 min, bright fluorescence was exclusively detected on NTR, indicating a preference of CyNT-F to covalently bind to neighboring proteins. In contrast, the noncovalent probe CyNT treated with NTR failed to fluorescently label proteins. Finally, the NTR-triggered cleavage of nitrobenzene and the covalent reaction of CyNT-F with the sulfhydryl group were validated by LC-MS spectrometry and ESI-MS spectrometry (Figures S22and S23), and the mechanism is illustrated in Figure 1G. Under

https://doi.org/10.1021/jacsau.4c00787
JACS Au 2024, 4, 4032−4042

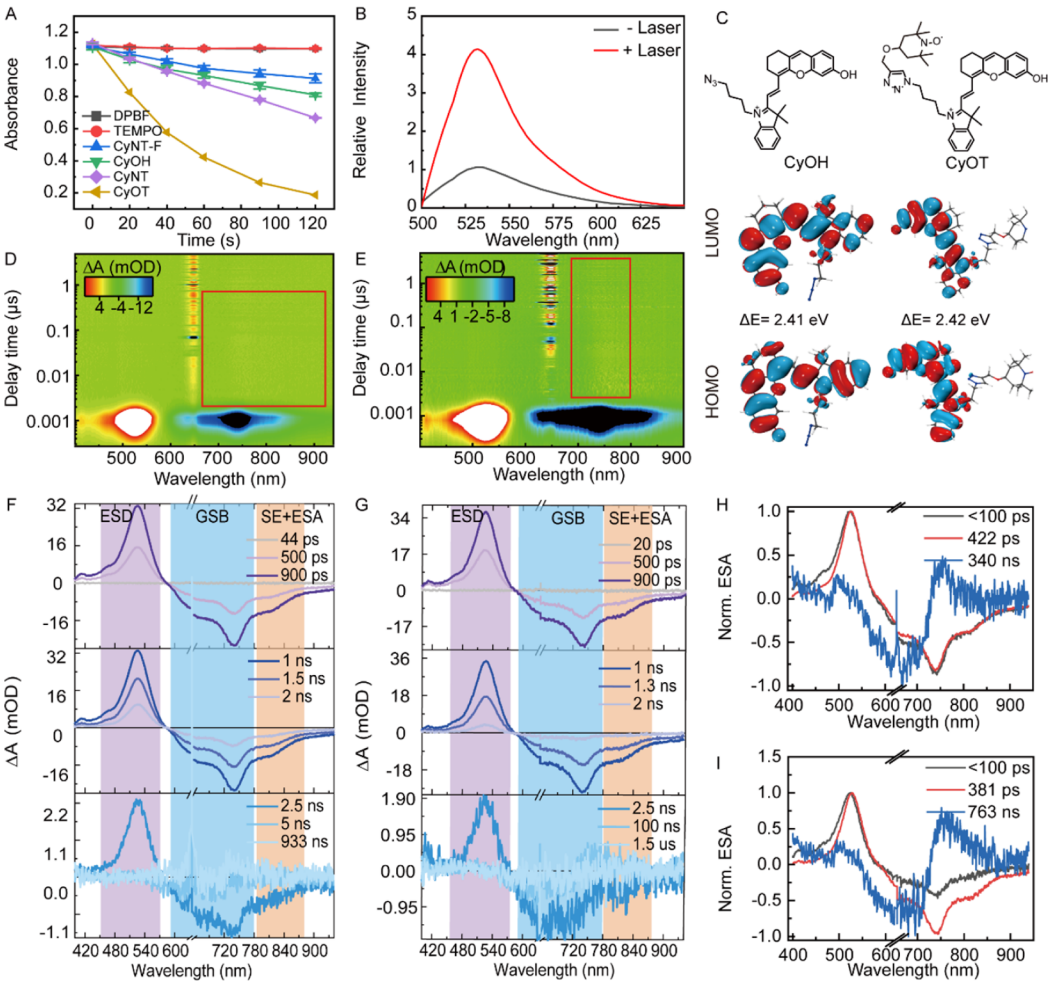

Figure 2. (A) Absorbance of DPBF at 415 nm in DMF with TEMPO, CyOH, CyOT, CyNT, and CyNT-F upon 655 nm laser irradiation at 6.37 mW/cm^2 (mean ± SD, n = 3). (B) Relative fluorescence intensity of SOSG after CyNT-F treated with NTR (λ_{Ex} = 480 nm). (C) Optimized molecular structures and calculated HOMO−LUMO energy gaps of CyOH and CyOT. (D) Time-resolved fluorescence spectra of CyOH. (E) Time-resolved fluorescence spectra of CyOT. (F) Transient absorption spectra of CyOH. (G) Transient absorption spectra of CyOT. (H) The evolution-associated decay spectra of CyOH. (I) The evolution-associated decay spectra of CyOT.

the catalysis of NTR, CyNT-F underwent a self-elimination reaction, liberating a highly reactive quinone methide group that was rapidly trapped by neighboring proteins to form a fluorescent adduct, thereby facilitating the generation of the fluorescence signal.

Next, the photodynamic performance of the four compounds (CyOH, CyOT, CyNT, and CyNT-F) was evaluated by employing 1,3-diphenylisobenzofuran (DPBF) as a singlet oxygen indicator. As depicted in Figure 2A, the absorbance at 415 nm of DPBF solution containing CyOT rapidly decreased by 83.6% within 120 s upon irradiation with a 655 nm laser, while there was only an 18.2% decrease in absorbance observed in the DPBF solution containing CyOH alone, which suggested that CyOT exhibited a higher singlet oxygen yield and photodynamic performance. In contrast, both CyNT and CyNT-F exhibited lower yields of singlet oxygen production, indicating that protection of phenolic hydroxyl groups not only quenches probe fluorescence but also inhibits singlet oxygen generation. Similarly, TEMPO did not induce a reduction in the absorbance of DPBF. Subsequently, the recovery of photodynamic performance upon the activation of CyNT-F by NTR was validated through the singlet oxygen detection probe SOSG (a singlet oxygen detection reagent). As depicted in Figure 2B, incubation of CyNT-F with NTR for 15 min followed by irradiation with a 655 nm laser for 1 min resulted in a 4.0-fold increase in the SOSG fluorescence intensity, indicating that the photodynamic properties of the probe were activated. Therefore, CyNT-F could serve as an activatable photosensitizer.

In order to gain a deeper understanding of the alterations induced by free radical modification, density functional theory calculations (DFT) were conducted at the B3YLP level to obtain the optimized singlet state geometries (S_1) and triplet state (T_1) by the time-resolved fluorescence spectra measurements of CyOH and CyOT. The energy gap values of CyOH and CyOT were nearly identical, providing evidence for their similar maximum emission peaks (Figure 2C). Subsequently, the nanosecond time-resolved transient absorption spectra of CyOH and CyOT were measured, as depicted in Figure 2D,E. Both spectra exhibited similar spectral characteristics, featuring prominent negative signals within the range of 600−800 nm, which corresponded to the peak positions observed in their respective steady-state absorption and fluorescence emission profiles. It should be noted that following the initial decay of GSB (ground state bleaching), SE (stimulated emission), and ESA (excited state absorption) signals around 550 nm within 2

https://doi.org/10.1021/jacsau.4c00787
JACS Au 2024, 4, 4032−4042

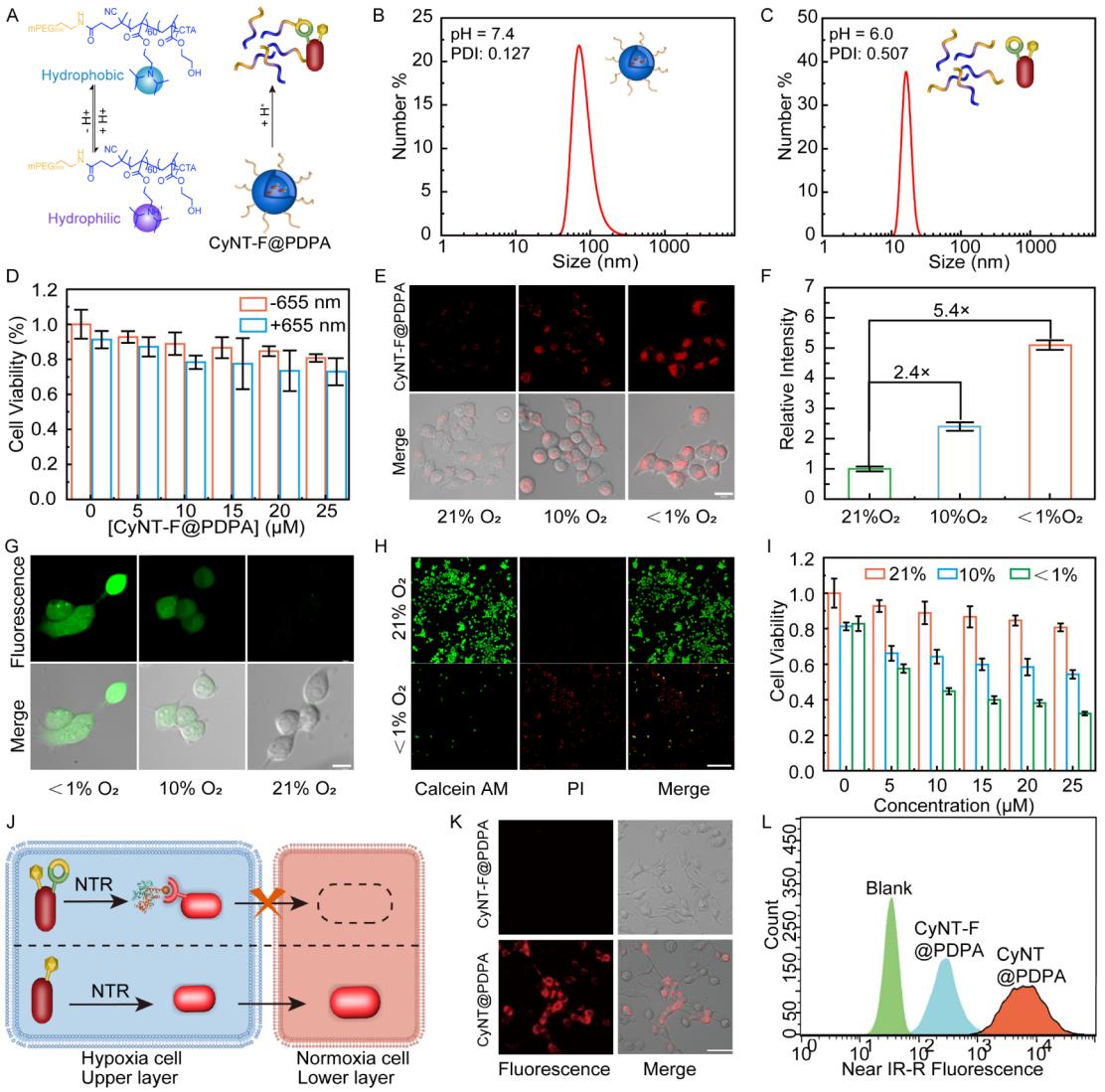

Figure 3. (A) Schematic diagram of nanomicelle dissociation. (B) Nanoparticle size of CyNT-F@PDPA at pH 7.4. (C) Nanoparticle size of CyNT-F@PDPA at pH 6.0. (D) Cell viability of CyNT-F@PDPA under a 655 nm laser and in darkness (mean ± SD, n = 3). (E) Fluorescence imaging of CyNT-F (red) in 4T1 cells at different O_2 concentrations (Scale bar: 20 μm). (F) Relative fluorescence intensity of CyNT-F (mean ± SD, n = 3) based on (E). (G) Detection of intracellular ROS production by DCFH-DA (green) in 4T1 cells (scale bar: 20 μm). (H) Live (green)/Dead (red) staining images of 4T1 cells under different oxygen contents after 655 nm laser irradiation (150 mW/cm^2, 655 nm laser for 5 min, scale bar: 200 μm). (I) Cytotoxicity of CyNT-F@PDPA with different oxygen contents (mean ± SD, n = 3). (J) The schematic illustration of the transwell migration experiment. (K) Fluorescence imaging (red: CyNT or CyNT-F) and (L) flow cytometry detection of lower cells in the transwell experiment (scale bar: 200 μm).

ns, persistent ESA signals were still observed in the transient absorption spectra of CyOH and CyOT between 700 and 850 nm over a time range of 0.01−1 μs.

The corresponding evolution process of the transient absorption spectra of CyOH and CyOT (Figure 2F,G) also revealed that the intense ESA signal near 550 nm was closely associated with the decay of GSB and SE signals between 600 and 800 nm, which exhibited rapid decay within 5 ns. The long-lived components, which were not observed in the time-resolved fluorescence spectra, may originate from the non-emissive triplet states of CyOH and CyOT. Furthermore, we constructed the evolution-associated decay spectra (EADS) of CyOH and CyOT by employing a combination of singular value decomposition (SVD) and global fitting techniques. As depicted in Figure 2H,I, both molecules exhibited three distinct components in their excited states; one component with a lifetime of less than 100 ps showed similar spectral features to the approximately 400 ps component. These components manifested discernible GSB and SE characteristics, accompanied by ESA occurring at around 550 nm. The ∼4 ns lifetimes obtained from time-resolved fluorescence spectroscopy can be attributed to higher-energy excited states and lower-energy fluorescence emitting states (S_1). Additionally, both molecules demonstrated a long-lived component between 600 and 700 nm, and 700 and 800 nm respectively, displaying GSB and ESA signals that can be assigned to triplet excited states. Moreover, it was noteworthy that the triplet state lifetime of CyOT (∼763 ns) significantly exceeded that of CyOH (∼340 ns), and an extended triplet lifetime leads to a more advantageous generation of singlet oxygen. Consequently, CyOT would exhibit a higher singlet oxygen yield and a lower fluorescence quantum yield compared to CyOH.

https://doi.org/10.1021/jacsau.4c00787
JACS Au 2024, 4, 4032−4042

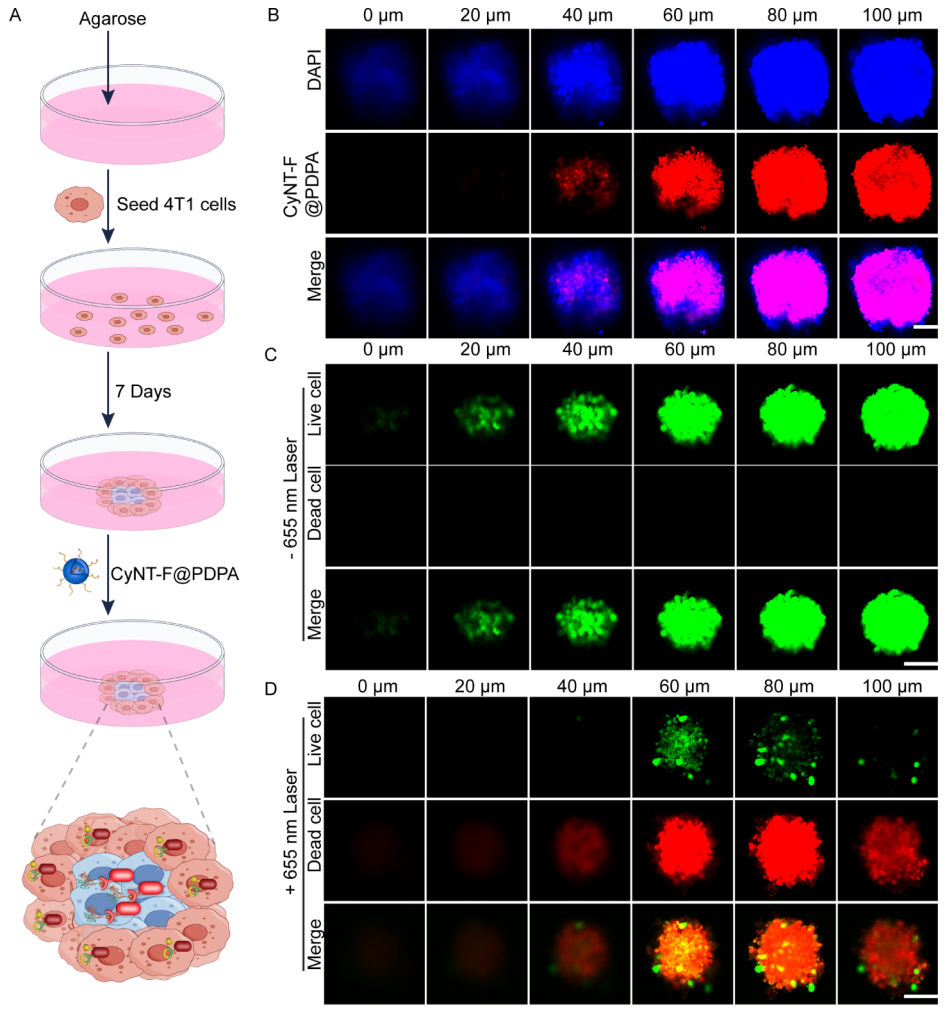

Figure 4. (A) Schematic diagram of the establishment of 3D multicellular spheroids. (B) Fluorescence imaging of CyNT-F@PDPA in 3D multicellular spheroids (blue: DAPI, red: CyNT-F). (C,D) Live (green)/Dead (red) fluorescence staining images of CyNT@PDPA under darkness and 655 nm irradiation (150 mW/cm^2 for 10 min). Scale bar = 100 μm.

This inference was in accordance with the properties of CyOH and CyOT as measured in Table S1 and Figures S24−S30.

To optimize tumor targeting, CyNT-F was encapsulated by the acid-responsive polymer (mPEG-*b*-PDPA: an acid-sensitive polymer that dissociates in pH 6.3 PBS solution[57,58]) via a coprecipitation method to obtain CyNT-F@PDPA (Figure 3A). The encapsulation efficiency of the probes was determined to be 30% using the absorption standard curve (Figures S31 and S32). CyNT-F@PDPA exhibited a uniform particle size distribution in PBS solution of pH 7.4 (Figure 3B). However, when exposed to PBS solution at pH 6.0, CyNT-F@PDPA displayed a distinct sign of an unstable aggregation state due to acid-triggered micelle dissociation (Figure 3C).

The phototoxicity and dark toxicity of CyNT-F@PDPA on 4T1 cells under normoxia were assessed using an MTT assay (Figure 3D). In the absence of the 655 nm laser, CyNT-F@PDPA exhibited minimal cytotoxicity, with cell viability remaining at approximately 80% even after exposure to the 655 nm laser at a concentration of 10 μM. These results suggested that CyNT-F@PDPA was highly biocompatible and could serve as an effective photosensitizer for activated PDT. Furthermore, we validated the activation process of endogenous NTR in 4T1 cells using confocal microscopy. Considering that the expression of NTR was closely associated with the level of hypoxia, 4T1 cells were preincubated at varying oxygen concentrations (21%, 10%, and <1% O_2) for a duration of 12 h to induce the upregulation of NTR. The control cells were incubated under normoxic conditions, subsequently, the cells were stained with CyNT-F@PDPA and incubated for an additional 4 h before imaging using confocal microscopy. As anticipated, no significant fluorescence was observed under normoxic conditions (21% O_2) (Figure 3E), which can be attributed to the low expression of NTR. However, a substantial increase in fluorescence signals (2.4-fold and 5.4-fold enhancement, respectively) was observed in the experimental group where NTR overexpression was induced by hypoxia (10%, <1% O_2) (Figure 3F). The fluorescence of CyNT-F@PDPA declined upon the addition of a NTR inhibitor (Figure S33). These results indicated that the fluorescence of CyNT-F@PDPA could be activated specifically by endogenous NTR in living cells. Subsequently, the photodynamic performance of CyNT-F@PDPA in hypoxia cells was evaluated by DCFH-DA. As depicted in Figure 3G, following the sequential incubation of 4T1 cells with CyNT-F@PDPA (10 μM containing CyNT-F) for 4 h, DCFH-DA (10 μM) for 15 min, and exposure to light for 5 min, negligible fluorescence was observed under

https://doi.org/10.1021/jacsau.4c00787
JACS Au 2024, 4, 4032−4042

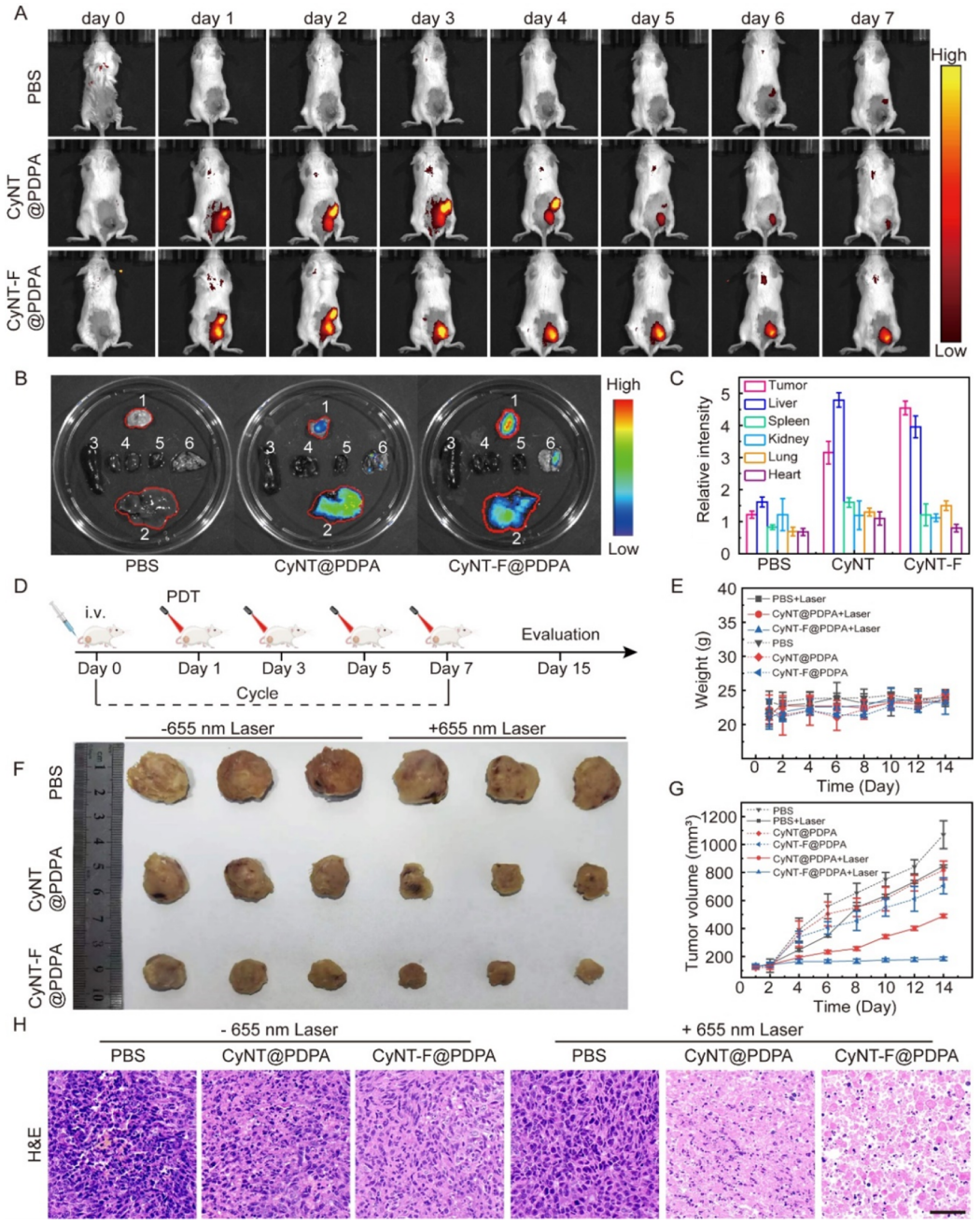

Figure 5. (A) Fluorescence imaging of hypoxia in 4T1 tumor-bearing mice. (B) Fluorescence imaging of mouse tumors and major organs at day 8 (1. tumor; 2. liver 3. spleen; 4. kidneys; 5. heart; 6. lungs). (C) Relative fluorescence intensity of mouse tumors and major organs at day 8 (mean ± SD, n = 3). (D) Experimental design of CyNT-F@PDPA-mediated PDT in 4T1 tumor-bearing mice. (E) Weight growth curves of tumor-bearing mice over 14 days (mean ± SD, n = 3). (F) Images of tumors after the treatment period. (G) Tumor growth curves of tumor-bearing mice over 14 days (mean ± SD, n = 3). (H) Hematoxylin and eosin (H&E) staining of tumors treated under different conditions. Scale bar = 50 μm.

normoxic conditions while intense green fluorescence was detected in hypoxic environments (10% and <1%), confirming the ability of the activated probe to generate ROS upon stimulation using a 655 nm laser.

Furthermore, we employed calcein AM and propidium iodide (PI) for live (green) and dead (red) cell discrimination, respectively. As depicted in Figure 3H, 4T1 cells cultured at varying oxygen concentrations were treated with CyNT-F@PDPA for 4 h followed by an additional incubation period of 12 h under continuous exposure to a 655 nm laser for 10 min. Subsequently, staining and imaging using calcein AM and PI were performed. In comparison to the light-irradiated normoxic group exhibiting strong green fluorescence with minimal red fluorescence, the hypoxic cells displayed intense red fluorescence along with limited green fluorescence upon treatment with CyNT-F@PDPA, indicating its effective tumor cell eradication capability under hypoxic conditions. To further assess the PDT efficacy of CyNT-F@PDPA in hypoxic cells, the MTT experiment was conducted, as depicted in Figure 3I; following 655 laser irradiations, the survival rate of cells in an anaerobic environment exhibited a significant decrease with increasing probe concentration.

Furthermore, a transwell migration assay was conducted to assess the covalent retention property of CyNT-F in cells

https://doi.org/10.1021/jacsau.4c00787
JACS Au 2024, 4, 4032−4042

(Figure 3J). First, CyNT@PDPA and CyNT-F@PDPA were separately incubated with the upper layer of cells that had been preincubated for 12 h under hypoxia conditions (<1%) to induce NTR overexpression. After 4 h incubation, the upper layer of cells was incubated in transwell chambers under normoxia for 24 h. Subsequently, imaging of the lower layer of cells was performed. The control group of CyNT@PDPA exhibited a robust fluorescent signal, indicating the presence of a substantial number of free probes within the cells following fluorescence activation (Figure 3K). These probes were expelled from the cells through cellular metabolism and subsequently taken up by the underlying layer of 4T1 cells. In contrast, no discernible fluorescence signal was observed for the CyNT-F@PDPA group. The flow cytometric analysis of the lower layer cells also revealed a significantly stronger fluorescence intensity for the noncovalent probe CyNT group compared to that for CyNT-F, suggesting that activated CyNT-F was difficult to metabolize and clear by cells (Figure 3L) and CyNT-F can be retained within cells over an extended period, enabling long-term imaging and PDT.

After verifying the exceptional performance of CyNT-F in terms of fluorescence activation and PDT in cellular environments, we proceeded to investigate the performance of CyNT-F in the imaging and PDT of hypoxic cells using a more complex and physiologically relevant 3D multicellular spheroid (Figure 4A). Initially, we cultured a 3D multicellular spheroid model with 4T1 cells in vitro. Subsequently, the 3D multicellular spheroids were stained with CYNT-F@PDPA (10 μM), incubated in a 21% oxygen environment for 24 h, and then subjected to DAPI staining for 1 h. Confocal *Z*-axis scanning was performed at depths ranging from 0 to 100 μm. As depicted in Figure 4B, the weak fluorescence images within the 0−40 μM range suggested that the extent of hypoxia in 3D multicellular spheroids was not severe. Conversely, the intense fluorescence signals observed at depths of 40−100 μm indicated the effective activation of CyNT-F by NTR overexpression within the hypoxia environment present inside the 3D multicellular spheroid. By virtue of its specific activation in the hypoxia region of the tumor spheroids, the ROS generation ability of CyNT-F@PDPA in the 3D multicellular spheroid was subsequently tested. As shown in Figure S34, at a scanning depth of 60 μm, CyNT-F was fully activated and highly efficiently generated ROS upon 655 nm laser irradiation. Finally, the PDT efficacy of CyNT-F@PDPA was evaluated. First, CyNT-F@PDPA was incubated with the 3D multicellular spheroids for 24 h under normoxia conditions. The light group underwent irradiation using a 655 nm laser for 10 min, while the control group did not receive any light exposure. Subsequently, the 3D multicellular spheroids were stained with calcein AM and PI, and subjected to confocal *Z*-axis scanning depth imaging as depicted in Figure 4C,D. The bright green fluorescence observed within a depth range of 0−100 μm in the control group indicated that CyNT-F@PDPA exhibited low dark toxicity. In contrast, the green fluorescence of tumor spheroids in the light group was greatly reduced in 0−100 μm, accompanied by a rapid increase in red fluorescence representing dead cells, suggesting significant cell death among hypoxia cells within the tumor spheroids. These findings demonstrate that CYNT-F@PDPA can eliminate cancer cells.

Building on the impressive performance of CyNT-F in cellular and 3D multicellular spheroid imaging as well as PDT, we further evaluated the probe's hypoxia imaging capabilities in BALB/c mice bearing 4T1 tumors. Specifically, PBS, CyNT@PDPA, and CyNT-F@PDPA were administered via tail vein injection to mice, which were then imaged for seven consecutive days before being sacrificed on day 8 for tumor and major organ imaging. As depicted in Figure 5A, fluorescence signals at wavelengths of 720−760 nm were observed in the tumor region of mice from both the CyNT-F@PDPA group and the CyNT@PDPA group 24 h after tail vein injection. This phenomenon can be attributed to the probe being activated by overexpressed NTR under hypoxia conditions, and the fluorescence signal was maintained for 7 days. In contrast, the fluorescence intensity of the tumor treated with CyNT@PDPA exhibited a rapid decline after 3 days. The fluorescence intensity of the tumors in different groups of mice was quantified over 7 days (Figure S35). After a 24 h period following drug administration, the tumor treated with CyNT-F@PDPA exhibited a fluorescence enhancement of 5.1-fold, while the tumor treated with the CyNT@PDPA group showed a fluorescence increase of 3.8-fold. With time progression, the fluorescence intensity in the CyNT@PDPA group displayed a continuous attenuation trend. However, the fluorescence intensity in the CyNT-F@PDPA group remained relatively stable for up to 4 days, and even on day 7, it still demonstrated a significant enhancement by approximately 3.7-fold compared to the baseline levels. In contrast, only a 2.0-fold increase in fluorescence remained observable in the CyNT@PDPA group at this point. These findings suggest that covalent photosensitizers effectively resist tumor cell metabolism and prolong their retention within tumors, which is supported by our fluorescence imaging results obtained from mouse tumors and major organs on day 8 (Figure 5B,C).

The PDT effect of the probe was evaluated by categorizing the tumors into six groups (PBS, PBS+655 nm laser, CyNT@PDPA, CyNT@PDPA+655 nm laser, CyNT-F@PDPA, and CyNT-F@PDPA+655 nm laser). Once the tumor volume reached 150 mm^3, the treatment regimen depicted in Figure 5D was followed, and each group was exposed to a 655 nm laser (150 mW/cm^2) for a duration of 15 min per treatment. Additionally, the PDT effect was evaluated based on the tumor volume growth and changes in the body weight of mice collected every 2 days. Figure 5E displayed negligible differences in mouse body weight between the PDT and PBS groups within a 14-day period, indicating that the treatment did not induce substantial harm to the mice. As illustrated in Figure 5F,G, compared to the PBS group alone, the tumor growth inhibition rate was approximately 21% in the PBS+PDT group. This disparity may be attributed to laser irradiation-induced thermal effects. CyNT@PDPA and CyNT-F@PDPA exhibited inhibition rates of 23% and 34%, respectively, compared with the PBS group. This could be attributed to dark toxicity resulting from extensive probe accumulation at the tumor site upon activation. Due to its covalent properties, CyNT-F@PDAP demonstrated enhanced accumulation efficacy leading to superior tumor inhibition rates when compared with CyNT@PDPA. Overall, the high postactivation accumulation and dark toxicity of CyNT-F@PDPA are advantageous for suppressing tumor growth. When tumors were irradiated with 655 nm (150 mW/cm^2) for 15 min, significant deceleration in the tumor growth rate was observed in both CyNT@PDPA and CyNT-F@PDPA treated groups. Particularly, the CyNT-F@PDPA+Laser group demonstrated a tumor growth inhibition rate of 82.8%, which was

https://doi.org/10.1021/jacsau.4c00787
JACS Au 2024, 4, 4032−4042

approximately four times higher than that observed in the PBS +Laser group.

To further substantiate this claim, euthanasia was performed at the end of the treatment to obtain four groups of organs through autopsy. These organs and tumors were subsequently processed into paraffin sections and stained with hematoxylin and eosin (H&E). As depicted in Figure S36, no discernible differences were observed in the organ morphology (heart, liver, spleen, kidneys, and lungs) between the PDT group and the PBS-treated group, suggesting that CyNT-F exhibited minimal toxicity toward normal tissues. But there was severely necrotic tumor tissue in the phototherapy group treated with CyNT-F@PDPA (Figure 5H). Collectively, these findings validate CyNT-F as a suitable agent for precise tumor imaging while effectively inhibiting tumor growth under light irradiation.

CONCLUSION

In conclusion, we have developed a novel NIR covalent photosensitizer for tumor imaging and therapeutic purposes, which is selectively activated in the hypoxia microenvironment of tumors and covalently binds to adjacent proteins. By forming covalent bonds with macromolecular proteins, the metabolism of photosensitizers within tumors is effectively delayed, leading to improved imaging sensitivity, enhanced fluorescence intensity, as well as increased accumulation and retention time in tumor tissues. The precise imaging-guided PDT utilizing this covalent photosensitizer demonstrates remarkable tumor inhibition while minimizing adverse effects compared to noncovalent photosensitizers. Importantly, the enzymatically triggered self-immobilization strategy of photosensitizers holds significant potential for achieving targeted cell ablation and clearance.

METHODS

Synthesis

The detailed synthesis method of the compounds is mentioned in the Supporting Information

Preparation of Nanomicelles

The polymer mPEG-*b*-PDPA (40 mg/mL) and the probe solution CyNT-F or CyNT (4 mg/mL) were added to a PBS solution (pH 7.4) under ultrasound conditions to self-assemble into nanomicelles through hydrophilic−hydrophobic interactions.

Cell Culture under Normoxic and Hypoxic Conditions

4T1 cells were cultured in DMEM (Dulbecco's modified Eagle medium) in an incubator containing 5% CO_2 at 37 °C. The DMEM contained 10% fetal bovine serum and 1% penicillin-streptomycin.

4T1 cells were seeded on a confocal culture dish and incubated in a cell culture incubator at a normal oxygen concentration for 12 h. Subsequently, the confocal culture dish was transferred to a hypoxic incubation bag (AnaeroPack) with varying oxygen concentrations. The cells were then incubated at 37 °C for 12 h to induce NTR overexpression.

Establishment of 3D Multicellular Spheroids

200 mg of agarose was dissolved in 20 mL of deionized water by heating. The hot agarose solution (150 μL per well) was transferred to a 48-well plate. Once agarose cools and solidifies, 4T1 cells were inoculated into each well at a density of 1×10^3 cells per well. 500 μL of the culture medium was added to each well and incubated for cell growth. The culture medium was refreshed every 3 days until the cells aggregate into spheroids.

ASSOCIATED CONTENT

Supporting Information

The Supporting Information is available free of charge at https://pubs.acs.org/doi/10.1021/jacsau.4c00787.

Materials and methods, synthetic procedures and characterization, detailed experimental procedures, and spectral data (PDF)

AUTHOR INFORMATION

Corresponding Author

Zhiai Xu − *School of Chemistry and Molecular Engineering, East China Normal University, Shanghai 200241, China;* orcid.org/0000-0002-4391-2507; Email: zaxu@chem.ecnu.edu.cn

Authors

Zifan Zhu − *School of Chemistry and Molecular Engineering, East China Normal University, Shanghai 200241, China*

Yun Feng − *School of Chemistry and Molecular Engineering, East China Normal University, Shanghai 200241, China*

Qiufen Tian − *School of Chemistry and Molecular Engineering, East China Normal University, Shanghai 200241, China*

Jiawen Li − *School of Chemistry and Molecular Engineering, East China Normal University, Shanghai 200241, China*

Chencong Liu − *School of Pharmacy, China Pharmaceutical University, Nanjing 211198, China; State Key Laboratory of Chemical Biology & Center of Pharmaceutics, Shanghai Institute of Materia Medica, Chinese Academy of Sciences, Shanghai 201203, China*

Yuchi Cheng − *State Key Laboratory of Precision Spectroscopy, East China Normal University, Shanghai 200241, China*

Sanjun Zhang − *State Key Laboratory of Precision Spectroscopy, East China Normal University, Shanghai 200241, China;* orcid.org/0000-0002-7377-2429

Yijing Dang − *School of Chemistry and Molecular Engineering, East China Normal University, Shanghai 200241, China*

Jing Gao − *State Key Laboratory of Chemical Biology & Center of Pharmaceutics, Shanghai Institute of Materia Medica, Chinese Academy of Sciences, Shanghai 201203, China*

Yi Lai − *State Key Laboratory of Chemical Biology & Center of Pharmaceutics, Shanghai Institute of Materia Medica, Chinese Academy of Sciences, Shanghai 201203, China*

Fan Zhang − *Department of Chemistry, Fudan University, Shanghai 200433, China;* orcid.org/0000-0001-7886-6144

Haijun Yu − *State Key Laboratory of Chemical Biology & Center of Pharmaceutics, Shanghai Institute of Materia Medica, Chinese Academy of Sciences, Shanghai 201203, China;* orcid.org/0000-0002-3398-0880

Wen Zhang − *School of Chemistry and Molecular Engineering, East China Normal University, Shanghai 200241, China; Shanghai Engineering Research Center of Molecular Therapeutics and New Drug Development, East China Normal University, Shanghai 200062, China;* orcid.org/0000-0001-7918-4065

https://doi.org/10.1021/jacsau.4c00787
JACS Au 2024, 4, 4032−4042

Complete contact information is available at:
https://pubs.acs.org/10.1021/jacsau.4c00787

Notes

The authors declare no competing financial interest.

■ ACKNOWLEDGMENTS

Financial support by the National Natural Science Foundation of China (no. 22074043, 22174047, and 32311530041) and the Science and Technology Commission of Shanghai Municipality (no. 23490712700) is greatly appreciated.

■ REFERENCES

(1) Pham, T. C.; Nguyen, V. N.; Choi, Y.; Lee, S.; Yoon, J. Recent Strategies to Develop Innovative Photosensitizers for Enhanced Photodynamic Therapy. *Chem. Rev.* **2021**, *121* (21), 13454−13619.
(2) Xie, J.; Wang, Y.; Choi, W.; Jangili, P.; Ge, Y.; Xu, Y.; Kang, J.; Liu, L.; Zhang, B.; Xie, Z.; He, J.; Xie, N.; Nie, G.; Zhang, H.; Kim, J. S. Overcoming Barriers in Photodynamic Therapy Harnessing Nano-Formulation Strategies. *Chem. Soc. Rev.* **2021**, *50* (16), 9152−9201.
(3) Li, X.; Kwon, N.; Guo, T.; Liu, Z.; Yoon, J. Innovative Strategies for Hypoxic-Tumor Photodynamic Therapy. *Angew. Chem., Int. Ed.* **2018**, *57* (36), 11522−11531.
(4) Hu, F.; Xu, S.; Liu, B. Photosensitizers with Aggregation-Induced Emission: Materials and Biomedical Applications. *Adv. Mater.* **2018**, *30* (45), 1801350.
(5) Zhao, J.; Wu, W.; Sun, J.; Guo, S. Triplet Photosensitizers: From Molecular Design to Applications. *Chem. Soc. Rev.* **2013**, *42* (12), 5323.
(6) Dolmans, D. E. J. G. J.; Fukumura, D.; Jain, R. K. Photodynamic Therapy for Cancer. *Nat. Rev. Cancer* **2003**, *3* (5), 380−387.
(7) Lovell, J. F.; Liu, T. W.; Chen, J.; Zheng, G. Activatable Photosensitizers for Imaging and Therapy. *Chem. Rev.* **2010**, *110* (5), 2839−2857.
(8) Liu, M.; Li, C. Recent Advances in Activatable Organic Photosensitizers for Specific Photodynamic Therapy. *ChemPluschem* **2020**, *85* (5), 948−957.
(9) Chen, H.; Bi, Q.; Yao, Y.; Tan, N. Dimeric BODIPY-Loaded Liposomes for Dual Hypoxia Marker Imaging and Activatable Photodynamic Therapy against Tumors. *J. Mater. Chem. B* **2018**, *6* (26), 4351−4359.
(10) Liu, Z.; Song, F.; Shi, W.; Gurzadyan, G.; Yin, H.; Song, B.; Liang, R.; Peng, X. Nitroreductase-Activatable Theranostic Molecules with High PDT Efficiency under Mild Hypoxia Based on a TADF Fluorescein Derivative. *ACS Appl. Mater. Interfaces* **2019**, *11* (17), 15426−15435.
(11) Piao, W.; Hanaoka, K.; Fujisawa, T.; Takeuchi, S.; Komatsu, T.; Ueno, T.; Terai, T.; Tahara, T.; Nagano, T.; Urano, Y. Development of an Azo-Based Photosensitizer Activated under Mild Hypoxia for Photodynamic Therapy. *J. Am. Chem. Soc.* **2017**, *139* (39), 13713−13719.
(12) Piao, W.; Tsuda, S.; Tanaka, Y.; Maeda, S.; Liu, F.; Takahashi, S.; Kushida, Y.; Komatsu, T.; Ueno, T.; Terai, T.; Nakazawa, T.; Uchiyama, M.; Morokuma, K.; Nagano, T.; Hanaoka, K. Development of Azo-Based Fluorescent Probes to Detect Different Levels of Hypoxia. *Angew. Chem.* **2013**, *125* (49), 13266−13270.
(13) Verwilst, P.; Han, J.; Lee, J.; Mun, S.; Kang, H.-G.; Kim, J. S. Reconsidering Azobenzene as a Component of Small-Molecule Hypoxia-Mediated Cancer Drugs: A Theranostic Case Study. *Biomaterials* **2017**, *115*, 104−114.
(14) Gerweck, L. E. The pH Difference between Tumor and Normal Tissue Offers a Tumor Specific Target for the Treatment of Cancer. *Drug Resist. Updat.* **2000**, *3* (1), 49−50.
(15) Han, K.; Wang, S.-B.; Lei, Q.; Zhu, J.-Y.; Zhang, X.-Z. Ratiometric Biosensor for Aggregation-Induced Emission-Guided Precise Photodynamic Therapy. *ACS Nano* **2015**, *9* (10), 10268−10277.
(16) Hu, W.; He, T.; Zhao, H.; Tao, H.; Chen, R.; Jin, L.; Li, J.; Fan, Q.; Huang, W.; Baev, A.; Prasad, P. N. Stimuli-Responsive Reversible Switching of Intersystem Crossing in Pure Organic Material for Smart Photodynamic Therapy. *Angew. Chem., Int. Ed.* **2019**, *58* (32), 11105−11111.
(17) Li, X.; Kolemen, S.; Yoon, J.; Akkaya, E. U. Activatable Photosensitizers: Agents for Selective Photodynamic Therapy. *Adv. Funct. Mater.* **2017**, *27* (5), 1604053.
(18) Sun, J.; Cai, X.; Wang, C.; Du, K.; Chen, W.; Feng, F.; Wang, S. Cascade Reactions by Nitric Oxide and Hydrogen Radical for Anti-Hypoxia Photodynamic Therapy Using an Activatable Photosensitizer. *J. Am. Chem. Soc.* **2021**, *143* (2), 868−878.
(19) Lai, Y.; Dang, Y.; Li, F.; Ding, C.; Yu, H.; Zhang, W.; Xu, Z. Reactive Glycolysis Metabolite-Activatable Nanotheranostics for NIR-II Fluorescence Imaging-Guided Phototherapy of Cancer. *Adv. Funct. Mater.* **2022**, *32* (23), 2200016.
(20) Xu, J.; Lai, Y.; Wang, F.; Zou, Z.; Pei, R.; Yu, H.; Xu, Z. Dual Stimuli-Activatable Versatile Nanoplatform for Photodynamic Therapy and Chemotherapy of Triple-Negative Breast Cancer. *Chin. Chem. Lett.* **2023**, *34* (12), 108332.
(21) Galland, M.; Le Bahers, T.; Banyasz, A.; Lascoux, N.; Duperray, A.; Grichine, A.; Tripier, R.; Guyot, Y.; Maynadier, M.; Nguyen, C.; et al. A "Multi-Heavy-Atom" Approach toward Biphotonic Photosensitizers with Improved Singlet-Oxygen Generation Properties. *Chem. − Eur. J.* **2019**, *25* (38), 9026−9034.
(22) Colvin, M. T.; Ricks, A. B.; Scott, A. M.; Co, D. T.; Wasielewski, M. R. Intersystem Crossing Involving Strongly Spin Exchange-Coupled Radical Ion Pairs in Donor−Bridge−Acceptor Molecules. *Sens. Actuators, B* **2012**, *116* (8), 1923−1930.
(23) Amemori, S.; Sasaki, Y.; Yanai, N.; Kimizuka, N. Near-Infrared-to-Visible Photon Upconversion Sensitized by a Metal Complex with Spin-Forbidden yet Strong S_0−T_1 Absorption. *J. Am. Chem. Soc.* **2016**, *138* (28), 8702−8705.
(24) Kamkaew, A.; Lim, S. H.; Lee, H. B.; Kiew, L. V.; Chung, L. Y.; Burgess, K. BODIPY Dyes in Photodynamic Therapy. *Chem. Soc. Rev.* **2013**, *42* (1), 77−88.
(25) Tian, J.; Zhou, J.; Shen, Z.; Ding, L.; Yu, J.-S.; Ju, H. A pH-Activatable and Aniline-Substituted Photosensitizer for near-Infrared Cancer Theranostics. *Chem. Sci.* **2015**, *6* (10), 5969−5977.
(26) Wu, X.; Li, H.; Lee, E.; Yoon, J. Sensors for In Situ Real-Time Fluorescence Imaging of Enzymes. *Chem* **2020**, *6* (11), 2893−2901.
(27) Wu, X.; Wang, R.; Kwon, N.; Ma, H.; Yoon, J. Activatable Fluorescent Probes for *in Situ* Imaging of Enzymes. *Chem. Soc. Rev.* **2022**, *51* (2), 450−463.
(28) Doura, T.; Kamiya, M.; Obata, F.; Yamaguchi, Y.; Hiyama, T. Y.; Matsuda, T.; Fukamizu, A.; Noda, M.; Miura, M.; Urano, Y. Detection of *LacZ*-Positive Cells in Living Tissue with Single-Cell Resolution. *Angew. Chem.* **2016**, *128* (33), 9772−9776.
(29) Iwashita, H.; Castillo, E.; Messina, M. S.; Swanson, R. A.; Chang, C. J. A Tandem Activity-Based Sensing and Labeling Strategy Enables Imaging of Transcellular Hydrogen Peroxide Signaling. *Proc. Natl. Acad. Sci.* **2021**, *118* (9), No. e2018513118.
(30) Li, Y.; Song, H.; Xue, C.; Fang, Z.; Xiong, L.; Xie, H. A Self-Immobilizing near-Infrared Fluorogenic Probe for Sensitive Imaging of Extracellular Enzyme Activity *in Vivo*. *Chem. Sci.* **2020**, *11* (23), 5889−5894.
(31) Liu, T.; Xia, X.; Wang, R.; Rong, X.; Su, Z.; Du, J.; Fan, J.; Peng, X.; Sun, W. A Fluorescent Chemosensor for Long-Term Tracking of Cancer Cell Metastasis and Invasion via Enzyme-Activated Anchoring. *Adv. Funct. Mater.* **2023**, *33* (48), 2304347.
(32) Obara, R.; Kamiya, M.; Tanaka, Y.; Abe, A.; Kojima, R.; Kawaguchi, T.; Sugawara, M.; Takahashi, A.; Noda, T.; Urano, Y. γ-Glutamyltranspeptidase (GGT)-Activatable Fluorescence Probe for Durable Tumor Imaging. *Angew. Chem., Int. Ed.* **2021**, *60* (4), 2125−2129.
(33) Shi, D.; Liu, W.; Gao, Y.; Li, X.; Huang, Y.; Li, X.; James, T. D.; Guo, Y.; Li, J. Photoactivatable Senolysis with Single-Cell Resolution Delays Aging. *Nat. Aging* **2023**, *3* (3), 297−312.

(34) Yu, Q.; Zhang, L.; Jiang, M.; Xiao, L.; Xiang, Y.; Wang, R.; Liu, Z.; Zhou, R.; Yang, M.; Li, C.; et al. An NIR Fluorescence Turn-on and MRI Bimodal Probe for Concurrent Real-time in Vivo Sensing and Labeling of β-Galactosidase. *Angew. Chem.* **2023**, *135* (46), No. e202313137.
(35) Kizaka-Kondoh, S.; Inoue, M.; Harada, H.; Hiraoka, M. Tumor Hypoxia: A Target for Selective Cancer Therapy. *Cancer Sci.* **2003**, *94* (12), 1021−1028.
(36) Zhou, J.; Schmid, T.; Schnitzer, S.; Brüne, B. Tumor Hypoxia and Cancer Progression. *Cancer Lett.* **2006**, *237* (1), 10−21.
(37) Zhou, Z.; Song, J.; Nie, L.; Chen, X. Reactive Oxygen Species Generating Systems Meeting Challenges of Photodynamic Cancer Therapy. *Chem. Soc. Rev.* **2016**, *45* (23), 6597−6626.
(38) Ogilby, P. R. Singlet Oxygen, There Is Indeed Something New under the Sun. *Chem. Soc. Rev.* **2010**, *39* (8), 3181−3209.
(39) Huang, L.; Zhao, S.; Wu, J.; Yu, L.; Singh, N.; Yang, K.; Lan, M.; Wang, P.; Kim, J. S. Photodynamic Therapy for Hypoxic Tumors: Advances and Perspectives. *Coord. Chem. Rev.* **2021**, *438*, 213888.
(40) Wei, F.; Rees, T. W.; Liao, X.; Ji, L.; Chao, H. Oxygen Self-Sufficient Photodynamic Therapy. *Coord. Chem. Rev.* **2021**, *432*, 213714.
(41) Hou, B.; Ye, J.; Li, J.; Xu, Z.; Yu, H. In-Situ Clickable Prodrug Nanoplatform Locally Activates T Lymphocytes to Potentiate Cancer Immunotherapy. *Nano Today* **2022**, *47*, 101661.
(42) Gao, J.; Hou, B.; Zhu, Q.; Yang, L.; Jiang, X.; Zou, Z.; Li, X.; Xu, T.; Zheng, M.; Chen, Y.-H.; et al. Engineered Bioorthogonal POLY-PROTAC Nanoparticles for Tumour-Specific Protein Degradation and Precise Cancer Therapy. *Nat. Commun.* **2022**, *13* (1), 4318.
(43) Liu, Q.; Tian, J.; Tian, Y.; Sun, Q.; Sun, D.; Wang, F.; Xu, H.; Ying, G.; Wang, J.; Yetisen, A. K.; Jiang, N. Near-Infrared-II Nanoparticles for Cancer Imaging of Immune Checkpoint Programmed Death-Ligand 1 and Photodynamic/Immune Therapy. *ACS Nano* **2021**, *15* (1), 515−525.
(44) Shen, Y.; Shuhendler, A. J.; Ye, D.; Xu, J.-J.; Chen, H.-Y. Two-Photon Excitation Nanoparticles for Photodynamic Therapy. *Chem. Soc. Rev.* **2016**, *45* (24), 6725−6741.
(45) Wang, C.; Zhao, X.; Jiang, H.; Wang, J.; Zhong, W.; Xue, K.; Zhu, C. Transporting Mitochondrion-Targeting Photosensitizers into Cancer Cells by Low-Density Lipoproteins for Fluorescence-Feedback Photodynamic Therapy. *Nanoscale* **2021**, *13* (2), 1195−1205.
(46) Li, T.; Hao, Y.; Dong, H.; Li, C.; Liu, J.; Zhang, Y.; Tang, Z.; Zeng, R.; Xu, M.; Chen, S. Target-Induced In Situ Formation of Organic Photosensitizer: A New Strategy for Photoelectrochemical Sensing. *ACS Sens.* **2022**, *7* (2), 415−422.
(47) Kim, J.; Lee, S.; Kim, Y.; Choi, M.; Lee, I.; Kim, E.; Yoon, C. G.; Pu, K.; Kang, H.; Kim, J. S. In Situ Self-Assembly for Cancer Therapy and Imaging. *Nat. Rev. Mater.* **2023**, *8* (11), 710−725.
(48) Castro, C. I.; Briceno, J. C. Perfluorocarbon-Based Oxygen Carriers: Review of Products and Trials. *Artif. Organs* **2010**, *34* (8), 622−634.
(49) Larue, L.; Moussounda Moussounda Koumba, T.; Le Breton, N.; Vileno, B.; Arnoux, P.; Jouan-Hureaux, V.; Boura, C.; Audran, G.; Bikanga, R.; Marque, S. R. A.; Acherar, S.; Frochot, C. Design of a Targeting and Oxygen-Independent Platform to Improve Photodynamic Therapy: A Proof of Concept. *ACS Appl. Bio Mater.* **2021**, *4* (2), 1330−1339.
(50) Feng, L.; Xie, R.; Wang, C.; Gai, S.; He, F.; Yang, D.; Yang, P.; Lin, J. Magnetic Targeting, Tumor Microenvironment-Responsive Intelligent Nanocatalysts for Enhanced Tumor Ablation. *ACS Nano* **2018**, *12* (11), 11000−11012.
(51) Lan, G.; Ni, K.; Xu, Z.; Veroneau, S. S.; Song, Y.; Lin, W. Nanoscale Metal−Organic Framework Overcomes Hypoxia for Photodynamic Therapy Primed Cancer Immunotherapy. *J. Am. Chem. Soc.* **2018**, *140* (17), 5670−5673.
(52) Tang, W.; Zhen, Z.; Wang, M.; Wang, H.; Chuang, Y.; Zhang, W.; Wang, G. D.; Todd, T.; Cowger, T.; Chen, H.; Liu, L.; Li, Z.; Xie, J. Red Blood Cell-Facilitated Photodynamic Therapy for Cancer Treatment. *Adv. Funct. Mater.* **2016**, *26* (11), 1757−1768.
(53) Zhang, X.; Tang, Q.; Sun, J.; Guo, Y.; Zhang, S.; Liang, S.; Dai, P.; Chen, X. Cellular-Scale Proximity Labeling for Recording Cell Spatial Organization in Mouse Tissues. *Sci. Adv.* **2023**, *9* (21), No. eadg6388.
(54) Liu, S.; Zhao, X.; Shui, S.; Wang, B.; Cui, Y.; Dong, S.; Yuwen, T.; Liu, G. PDTAC: Targeted Photodegradation of GPX4 Triggers Ferroptosis and Potent Antitumor Immunity. *J. Med. Chem.* **2022**, *65* (18), 12176−12187.
(55) Nguyen, V.-N.; Yan, Y.; Zhao, J.; Yoon, J. Heavy-Atom-Free Photosensitizers: From Molecular Design to Applications in the Photodynamic Therapy of Cancer. *Acc. Chem. Res.* **2021**, *54* (1), 207−220.
(56) Xu, F.; Ge, H.; Xu, N.; Yang, C.; Yao, Q.; Long, S.; Sun, W.; Fan, J.; Xu, X.; Peng, X. Radical Induced Quartet Photosensitizers with High $^1O_2$ Production for in Vivo Cancer Photodynamic Therapy. *Sci. China: Chem.* **2021**, *64* (3), 488−498.
(57) Hou, B.; Zhou, L.; Wang, H.; Saeed, M.; Wang, D.; Xu, Z.; Li, Y.; Yu, H. Engineering stimuli-activatable boolean logic prodrug nanoparticles for combination cancer immunotherapy. *Adv. Mater.* **2020**, *32* (12), 1907210.
(58) Gao, J.; Jiang, X.; Lei, S.; Cheng, W.; Lai, Y.; Li, M.; Yang, L.; Liu, P.; Chen, X.-h.; Huang, M.; et al. A region-confined PROTAC nanoplatform for spatiotemporally tunable protein degradation and enhanced cancer therapy. *Nat. Commun.* **2024**, *15* (1), 6608.

https://doi.org/10.1021/jacsau.4c00787
JACS Au 2024, 4, 4032−4042